Journal of Materials Research and Technology 30 (2024) 9148–9157

Contents lists available at ScienceDirect

Journal of Materials Research and Technology

journal homepage: www.elsevier.com/locate/jmrt

# Reversing relaxation-induced embrittlement by high-temperature thermal cyclic annealing in Zr-based metallic glass

Jingxian Cui, Qiang Luo *, Zhengguo Zhang, Jincan He, Qianzi Yang, Baolong Shen **

*School of Materials Science and Engineering, Jiangsu Key Laboratory for Advanced Metallic Materials, Southeast University, Nanjing, 211189, China*

ARTICLE INFO

*Keywords:*
Bulk metallic glass
High-temperature thermal cycling
Plastic deformation
Nanoscale creep deformation
Hardness fluctuations

ABSTRACT

Annealing usually induces structural relaxation and reduction of liquid-like regions, leading to embrittlement in bulk metallic glasses (BMGs). Here, we find that the short-term high-temperature thermal cycling (HTC) annealed $Zr_{41.2}Ti_{13.8}Cu_{12.5}Ni_{10}Be_{22.5}$ (Vit1) BMG shows an improved plasticity without sacrificing their yield strength. And only relaxation behavior with increased hardness is observed after HTC, which is different from the rejuvenation effect usually observed in cryogenic thermal cycling (CTC). We revealed that this embrittlement reversal is attributed to enhanced fluctuations of full width at half maximum (FWHM) of the hardness' distribution at micrometer and larger scales induced by short-term HTC. The enhanced fluctuations of mechanical heterogeneities across the diameter on a cross-section of the short-term HTC sample may increase the number and decrease the size of shear transformation zones (STZs) activated at high stress and promote the deflection of shear bands (SBs) during their propagation to form multiple SBs. The enhanced plasticity after HTC induced relaxation contradicts the common sense that relaxation accompanying with annihilation of free volume or liquid-like region usually causes embrittlement. Present results indicate that short-term HTC could be a powerful mean to tune the mechanical performance, shedding new lights on the interplay among relaxation, mechanical/structural heterogeneity, and plasticity of MGs.

## 1. Introduction

Bulk metallic glasses (BMGs) have been actively studied due to their unique disordered structure with complex spatial heterogeneity at different length scales and remarkable mechanical, magnetic, and chemical attributes [1–4]. However, one of the main impediments to wider structural use of BMGs is their intrinsic brittleness, that is, they generally fail catastrophically under unconstrained loading by forming nanoscale shear bands (SBs) at room temperature [5–7]. Understanding atomic-scale deformation mechanism and overcoming the poor plasticity are long-standing challenges in BMGs field. Different from many conventional crystalline alloys, in which annealing is widely used to enhance the mechanical properties, annealing usually induces severe embrittlement in BMGs owing to annihilation/reduction of free volume ($V_f$)/liquid like zones, increased shear modulus, decreased Poisson's ratio [8,9]. Annealing embrittlement was also related closely to reduced shear band activity [10]. And it is reported that the annealing induced ductile-brittle transition arises from the transition of shear band nucleation mode, the nucleation site density and the nucleation rate [11]. In fact, annealing embrittlement sensitivity varies among various BMGs and relates closely to the degree of order and fragility [8]. Fragile BMGs are found to be more prone to relaxation-induced embrittlement than stronger glasses [8]. Since it is hard to obtain improved plasticity in annealed MG state, introducing nano-crystalline(s) by isothermal annealing was adopted to enhance ductility in a few BMGs systems [12–14]. But it is of great challenges in controlling number, microstructure and size distributions of nano-crystalline phases (which are sensitive to the alloy's composition and annealing conditions) to enhance the plasticity.

Therefore, much current research turns to other strategies to improve general plasticity of BMGs, such as tuning chemical composition, irradiation, elastostatic loading, shot peening and cryogenic thermal cycling (CTC) treatment by enhancing the structural heterogeneity [15–17]. Among these methods, CTC is widely used due to the advantage of controllable, non-destructive features and no shape-changes [17]. It is worth noting that even though CTC is initially aimed at rejuvenating MGs, later investigations indicate that CTC can also induce relaxation and oscillatory (rejuvenation-relaxation transition) behavior [18]. It has

* Corresponding author.
** Corresponding author.
*E-mail addresses:* q.luo@seu.edu.cn (Q. Luo), blshen@seu.edu.cn (B. Shen).

https://doi.org/10.1016/j.jmrt.2024.06.013
Received 20 March 2024; Received in revised form 28 May 2024; Accepted 3 June 2024
Available online 4 June 2024

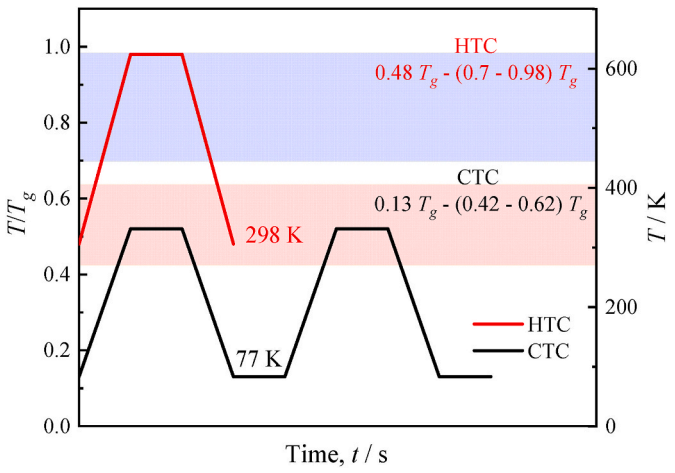


**Fig. 1.** Schematic diagram of the HTC and CTC process.

been verified that the rejuvenation process induced by CTC comes mainly from local atomic motion in loosely packed regions (LPRs), while the cooperative motion of atoms in densely packed regions (DPRs) is responsible for the other evolution path, i.e., relaxation [19]. Usually, to reduce the impact of structural relaxation during CTC, the upper temperature range of CTC is 0.42–0.62 $T_g$ ($T_g$ is the glass transition temperature) while the lower temperature is ordinarily set at the liquid-nitrogen temperature (77 K), which increases the complexity and cost of heat treatment [20]. Recently, rejuvenation induced by CTC is found to decay over about one week at room temperature after CTC in a series of Pd, Pt, Ti, or Zr-based glasses, returning the properties to those of the as-cast glass [21]. The reversion of CTC-induced properties implies a structural memory analogous to that of anelasticity, which are induced by largely uniaxial stresses on the sample [21].

Herein, we propose an easy-to-operate high-temperature thermal cycling (HTC) annealing as a novel strategy and investigate the effects of HTC with different sub-$T_g$ isothermal annealing intervals on plastic deformation, nanoscale creep deformation, structural and hardness fluctuations of $Zr_{41.2}Ti_{13.8}Cu_{12.5}Ni_{10}Be_{22.5}$ (Vit1) BMG. Contrast with conventional annealing experiments using from tens of minutes to several hours, rapid heating/cooling coupled with short-term isothermal annealing for 0.5 min and 1 min were included in present study. Surprisingly, enhanced plastic strain ($\varepsilon_p$) is obtained without sacrificing yield strength ($\sigma_y$) after HTC with isothermal annealing for 0.5 min at different temperatures. It is found that short-term HTC leads to structural relaxation instead of rejuvenation and promotes larger fluctuations of hardness, activates more defects, increases the number and decreases the size of shear transformation zones (STZs), thus reversing the relaxation-induced embrittlement. The correlations between structural heterogeneity and plastic deformation and creep deformation are also discussed. This present work opens avenues to improve mechanical properties and sheds new lights on the interplay among relaxation, mechanical heterogeneity, and plasticity of metallic glasses.

## 2. Experimental method

Master alloy with nominal compositions of $Zr_{41.2}Ti_{13.8}Cu_{12.5}Ni_{10}Be_{22.5}$ (Vit1) was prepared by arc melting high purity elements under Ti-gettered high purity argon, followed by die-casting into cooled

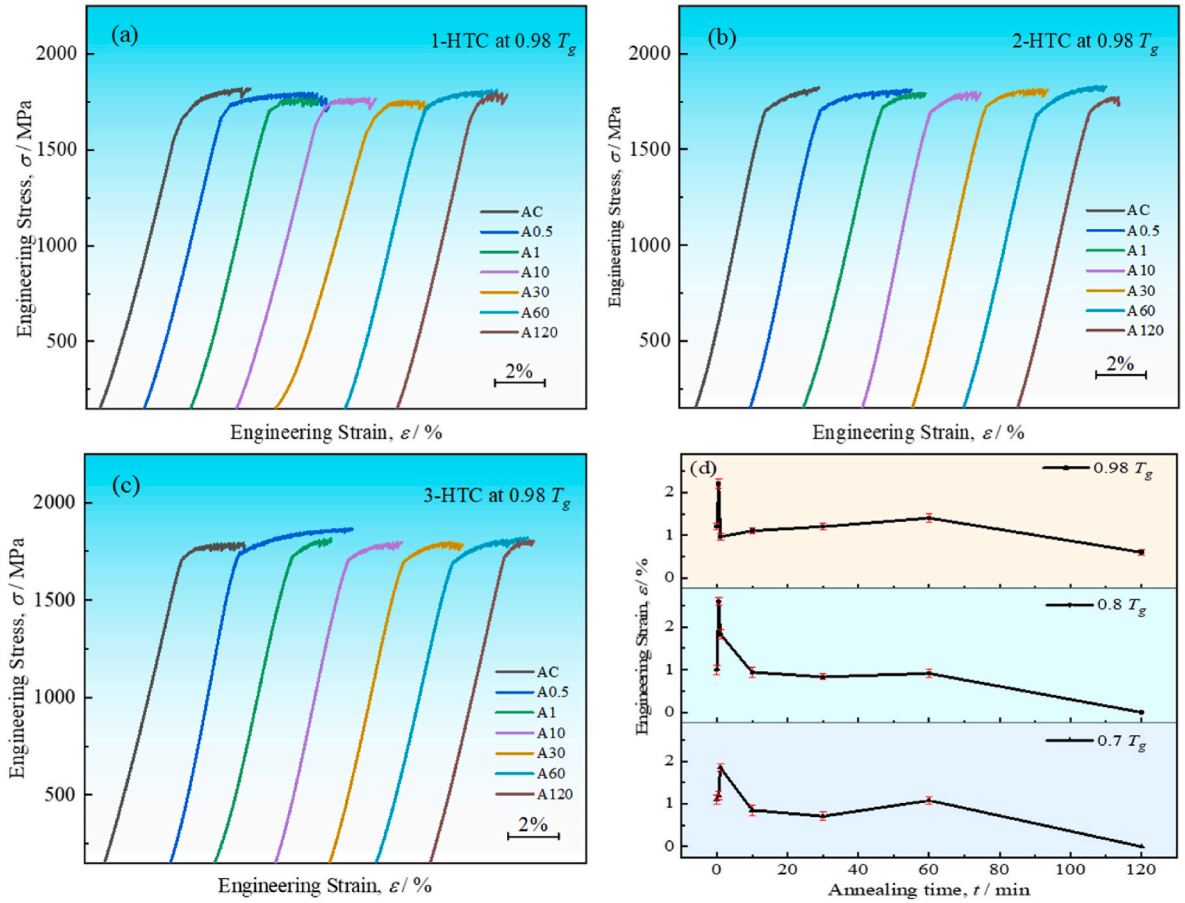


**Fig. 2.** (a–c) Three replicas of representative engineering stress-strain curves of Vit1 samples before and after HTC treatment at 0.98 $T_g$; (d) variation of $\varepsilon_p$ with error bars of AC and HTC treated Vit1 BMGs.

copper molds with a diameter of 3 mm. The specimens with aspect ratio of 2 (6 mm height and 3 mm diameter) were cut from the rod samples using a low-speed diamond cutting machine (SYJ-150) and their ends were then carefully polished to obtain parallel surfaces. HTC treatment with different thermal temperatures (0.98, 0.8 and 0.7 $T_g$) were applied in a high vacuum annealing furnace. In HTC, after the furnace heating to required temperatures, sealed samples were put into the furnace immediately and then annealed for 0.5 min, 1 min, 10 min, 30 min, 60 min and 120 min, followed by instantly immersed in water. The schematic diagram of the HTC process is shown in Fig. 1. Temperature error of the furnace was ±3 k. The as-cast and HTC treated samples with isothermal annealing for 0.5 min, 1 min, 10 min, 30 min, 60 min and 120 min are denoted as AC, A0.5, A1, A10, A30, A60 and A120 samples, respectively.

Compression tests were carried out using a Sans 5305 testing machine with a strain rate of $1 \times 10^{-4}$ $s^{-1}$. Three samples were tested for each condition to ensure repeatability. Surface morphology of deformed samples after fracture was analyzed by scanning electron microscopy (SEM, Sirion 200, FEI). The thermal properties were examined by differential scanning calorimeter (DSC, Netzsch 404 F3) at a heating rate of 20 K/min. In order to measure the relaxation enthalpy ($\Delta H_{rel}$), a second run under the same experimental settings was carried out right after the first heating process, and used as the baseline to be subtracted from the first DSC curve. 5 samples for each condition were tested to assess the reproducibility of $\Delta H_{rel}$ measurements. High-resolution transmission electron microscopy (HRTEM, Talos F200X) analysis were carried out to observe micro-structural changes before and after sub-$T_g$ isothermal annealing. Samples for HRTEM analysis were thinned by ion milling method (Gatan Inc., PIPS-M691) under liquid nitrogen cooling condition. For high angle annular dark-field (HAADF) imaging, a probe semi-convergence angle of 10.5 mrad and collection semi-angle of 58–200 mrad were used.

Nanoindentation tests were performed using a NanoTest Vantage (Micro Materials Ltd) with a standard Berkovich diamond indenter under load control model to study the creep deformation and cumulative distribution of hardness ($H$) and modulus ($E_r$). Nanoscale creep measurements were conducted with loading and unloading rates of 0.5, 10 and 50 mN/s. The maximum load ($P_{max}$) was 50 mN and the holding time at $P_{max}$ is 120 s. For cumulative distribution calculation, the loading and unloading rates of 1 mN/s were applied and the holding time is 2 s. For each sample and loading rate, five effective indentation tests were performed.

## 3. Results

### 3.1. Effect of annealing time on compressive plasticity

Typical engineering stress-strain curves of Vit1 sample before and after HTC treatment at 0.98 $T_g$ are shown in Fig. 2(a–c). During loading in compression, Vit1 BMG suffers from extreme shear localization in narrow shear bands (SBs), which leads to local heating and softening [22]. From the figure, it can be seen that sub-$T_g$ isothermal annealing for longer than 10 min leads to reduction of plasticity, as observed in many other reports [23]. Surprisingly, the plasticity is enhanced obviously after HTC with short-term isothermal annealing for 0.5 and 1 min at different annealing temperatures. The $\varepsilon_p$ of annealed samples shows a distinct peak at a short time of 0.5 min when annealing at 0.98 $T_g$ or 0.8 $T_g$. Improved $\varepsilon_p$ of 2.2% is achieved through annealing at 0.98 $T_g$ when annealing time is 0.5 min. The values of $\varepsilon_p$ with error bars of these samples are plotted in Fig. 2 (d). As shown in Fig. 2 (b), a slightly longer annealing time (1 min) is needed to obtain the maximum $\varepsilon_p$ when annealing temperature of 0.7 $T_g$. Different from variation of plastic strain ($\varepsilon_p$) with annealing time, yield strength ($\sigma_y$) remains almost unchanged about 1700 MPa. Since $\varepsilon_p$ changing with HTC duration is the same, 0.98 $T_g$ was chosen as the following HTC temperature in this paper.

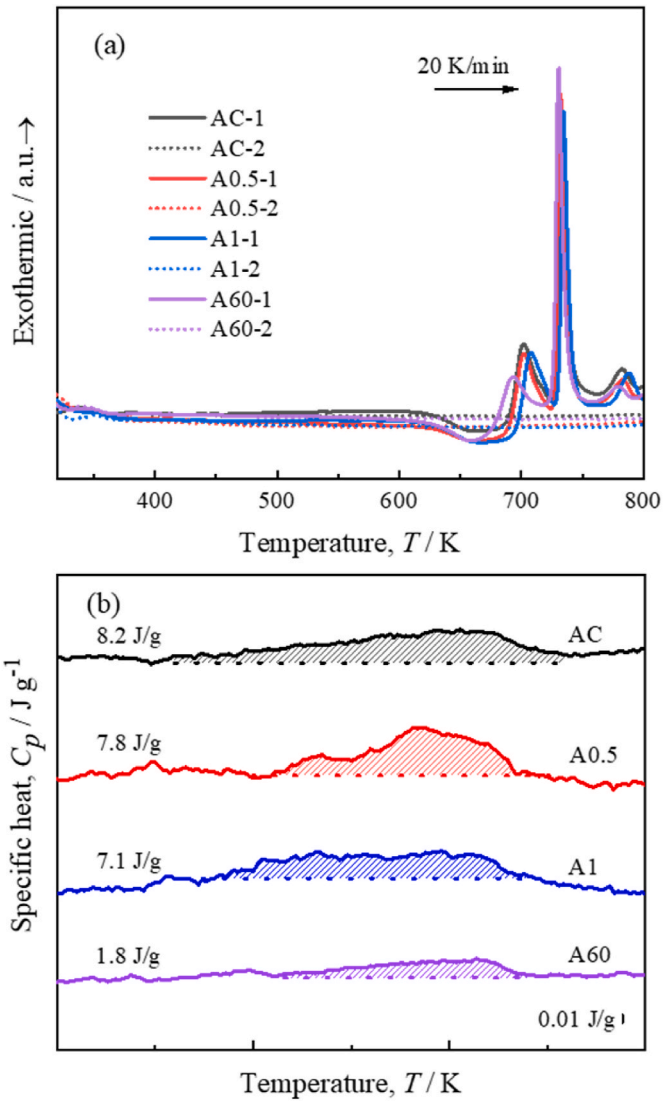


**Fig. 3.** (a) Thermograms of the first and second heating curves of the AC, A0.5, A1 and A60 samples with HTC treatment at 0.98 $T_g$. The solid lines represent the first heating curves and the dashed lines represent the second heating curves; (b) the relaxation enthalpy of AC, A0.5, A1 and A60 samples with HTC treatment at 0.98 $T_g$.

Thermograms of Vit 1 samples before and after HTC treatment at 0.98 $T_g$ were also investigated. The solid lines in Fig. 3 (a) present DSC curves of Vit 1 BMG under different HTC duration, respectively. The corresponding $T_g$ before and after HTC are approximately 623 K, indicating that HTC had little effect on the thermal stability of the Vit 1 BMG. However, the relaxation enthalpy ($\Delta H_{rel}$) calculated from the DSC curves before and after HTC are differed. From Greer's study [17], the sample was crystallized after the first DSC heating run on each sample. A second run on the now-crystalline sample, with the same heating procedure as the first run, was used to generate the baseline for subtraction from the first run. The relaxation enthalpy ($\Delta H_{rel}$) was then calculated as the area below the glass transition and presented in Fig. 3 (b) by the shaded area below the horizontal dashed line. The values of $\Delta H_{rel}$ gradually decreases with increasing isothermal annealing time increasing from 0.5 min to 120 min. It is indicative of relaxation instead of rejuvenation after HTC. The decreased $\Delta H_{rel}$ is acknowledged as the state of lower energy and more ordered structure, generally corresponds to the worsen plasticity. However, the AC sample does not exhibit the largest $\varepsilon_p$ although it shows the largest value of $\Delta H_{rel}$. This inconsistence has also been reported by other researchers [17,24], indicating that the

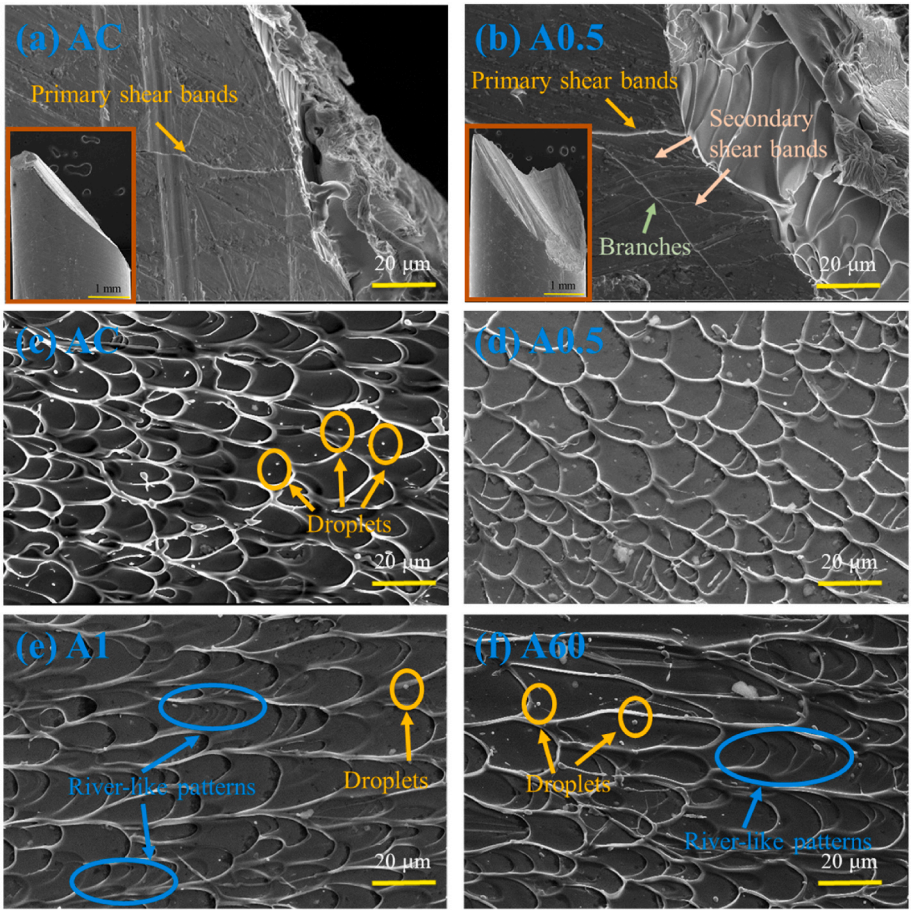


**Fig. 4.** SEM images of shear bands of (a) AC, (b) A0.5 samples with HTC treatment at 0.98 $T_g$; insets in (a–b) show lateral surface of the corresponding samples; SEM images of fracture morphology of (c) AC, (d) A0.5, (e) A1 and (f) A60 samples with HTC treatment at 0.98 $T_g$.

origins of structural changes affecting mechanical properties may not entirely be the same of those affecting the thermal behavior.

To clarify underlying mechanisms of the reversal of relaxation-induced embrittlement upon HTC, the lateral surface morphology and the fracture surface morphology of the AC and annealed samples were obtained and showed in Fig. 4. For the AC sample (inset in Fig. 4 (a)), only one primary SBs marked by the arrow, crossing through the sample, can be found, causing immediate failure. However, numerous shear bands reappear in the samples for A0.5 sample (inset in Fig. 4 (b)), which is consistent with the better $\varepsilon_p$ in A0.5 sample. Besides, secondary shear bands and branches are formed, and more importantly, the intersections of shear bands are even more abundant. All fracture surfaces show vein-like patterns, which reflect typical shear failure mode attributing to decreased viscosity during deformation [25]. Shear bands are similar to thin viscous layers existing between two parallel plates, on which shallow cavities will form and then the bridges between them break during shear deformation, resulting in vein-like patterns [26]. Besides, Argon et al. found that, during shear deformation of BMGs, the release of high elastic energy derived from shear bands will result in local softening or melting, and the softened or melted regions in shear bands are easy to flow, thus forming vein-like patterns [27]. There are also some molten droplets on fracture, arising from accumulated elastic energy induced by significant increase of temperature during the extension of shear bands on lateral surface [28,29]. Density of vein patterns plays an important role in plasticity and greater density of vein patterns usually means comparatively good plasticity [30]. As shown in Fig. 4 (b), the fracture of A0.5 exhibits the most regular and well-developed vein-like patterns. Besides, its shear bands are denser and more highly-branched than those of the as-cast alloy, indicating better plasticity. With increasing annealing time, the temperature increases due to adiabatic heating generated by large residual strain energy and SBs quickly turn into viscid matter. Therefore, ridges and rivers instead of perfect veins are formed on fracture surface subsequently. As shown in Fig. 4 (c-d), A1 and A60 samples show similar river-like patterns, leading to catastrophic fracture [23]. This is the reflection of low plasticity. Therefore, the result of fracture morphology variation is consistent with that of compressive stress-strain tests.

Creep strain rate sensitivity ($m$) and STZ volumes ($\Omega$) are further determined to understand the deformation mechanism and shown in Fig. 5. The $m$ was derived by Ref. [31]:

$$\mathrm{m} = \partial \ln \mathrm{H} / \partial \ln \varepsilon \tag{1}$$

where $H$ is the hardness and $\varepsilon$ the equivalent strain rate.

$$\varepsilon = \dot{\mathrm{P}} / 2\mathrm{P} \tag{2}$$

where $P$ is the applied force, $\dot{P} = dP/dt$. The values of $m$ for AC, A0.5 and A60 samples are 0.02044, 0.02112 and 0.04466, respectively. It has been proposed that the flow is inhomogeneous non-Newtonian for $m < 1$, meaning that the forced flow is achieved by sudden and localized atomic rearrangement [32]. The STZs volume ($\Omega$), shown in Fig. 5 (b), can be estimated based on cooperative shear model (CSM) [33]:

$$\Omega = \frac{\tau_C \sqrt{3} k_B T}{2mHR\xi G_0 \gamma_C^2 (1-\tau_{CT}/\tau_{C0})^{1/2}} \tag{3}$$

where $k_B$ is the Boltzmann constant and $T$ the temperature. $\tau_C$ and $G_0$ are threshold shear resistance and shear modulus at 0 K, respectively. The

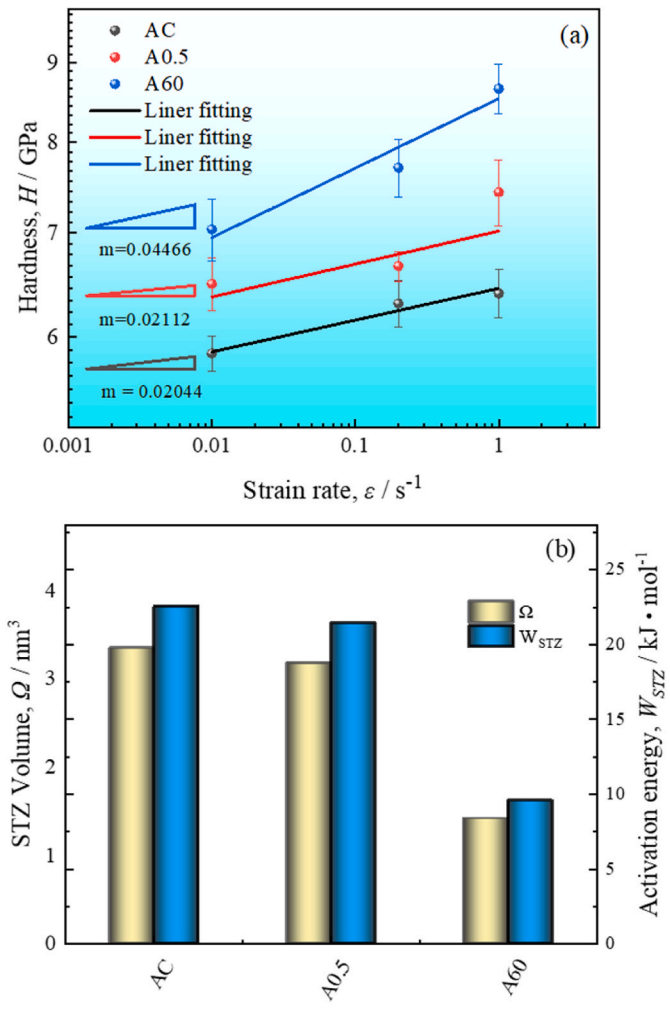


**Fig. 5.** (a) Determination of rate sensitivity $m$ of hardness and (b) STZ volume ($\Omega$) and activation energy ($W_{STZ}$) of AC, A0.5 and A60 samples with HTC treatment at 0.98 $T_g$.

constants of $R$, $\xi$ and $\gamma_C$ are equal to 0.25, 3 and 0.027, respectively. The value of $\tau_{CT}/\tau_{C0}$ at a certain $T$ can be estimated by the following equation [33]:

$$\frac{\tau_{CT}}{\tau_{C0}} = \frac{\gamma_{C0} - \gamma_{C1}\left(T/T_g\right)^{2/3}}{\tau_C/G_0} \tag{4}$$

the value of $\gamma_{C0}$ is 0.036 ± 0.002, $\gamma_{C1}$ is 0.016 ± 0.002. Normally, the formation of STZs is associated with STZs activation energy ($W_{STZ}$). For an STZ at finite stress, $0 < \tau_{CT} < \tau_{C0}$, $W_{STZ}$ can be defined as [34]:

$$W_{STZ} = 4RG_0\gamma_C^2\xi(1-\tau_{CT}/\tau_{C0})^{3/2}\Omega \tag{5}$$

activation volume $\Omega$ is thus calculated as 3.35 $nm^3$ for AC, 3.18 $nm^3$ for A0.5, and 1.42 $nm^3$ for A60 sample according to Eq. (3), which are in the same range as reported previously in experimental study and simulation [33,34]. As shown in Fig. 5 (b), potential energy barrier $W_{STZ}$ for an un-sheared STZ is in proportion to $\Omega$ and correlates with redistribution of atoms in a dispersed volume under external load. Generally, STZs consists of a few atoms to a few hundred atoms [35]. The decrease of $\Omega$ with annealing time is due to the densification effect, which cannot illustrate the enhancement of plasticity after short-term HTC.

### 3.2. Structural heterogeneities and mechanical fluctuations at different scales

It is well accepted that enhancing structural inhomogeneity is effective in facilitating local plastic events thus improving the plasticity of BMGs. Typical routes, such as cryogenic thermal cycling (CTC), elastic loading, severe plastic deformation, usually accompany the enhanced spatial heterogeneity with an increased fraction of liquid-like regions [17]. To understand the mechanism of plastic deformation, structural/mechanical heterogeneities at different length scales were investigated for present samples. Fig. 6(a–c) are HRTEM images for the AC, A0.5 and A60 samples, with corresponding selected area electron diffraction (SAED) patterns shown in insets. Homogeneous mazelike features of the phase-contrast HRTEM images show a fully amorphous structure without any crystalline phase. Besides, the diffuse halo rings of SAED patterns suggest amorphous structure before and after HCT treatment. Autocorrelation function (ACF) was carried out to quantitatively analyze effect of HCT on local crystal-like ordering (CLO). As shown in Fig. 6(d–f), total fraction of CLO structures is 8% in the AC sample, 17% in the A0.5 sample and 7% in the A60 sample. It indicates that short-term HTC promotes the formation of the CLO structures and enhances nanoscale structural heterogeneities. To explore possible chemical or density fluctuations in nanoscale, high-resolution HAADF-TEM measurements were performed and shown in Fig. 6(g–i). It is generally believed that the dark field enjoys lower density and loosely packed local configuration, corresponding to liquid-like regions or soft regions. In contrast, the bright field are composed of densely packed atoms, namely solid-like or hard regions [36]. From the figure, no apparent contrast difference can be detected among the as-cast and annealed Vit1 BMGs. Besides, the mappings of elements (Fig. 6(j–l)) show a homogeneous distribution, and a visible correlation between chemical variation and heterogeneities could not be detected.

Nanoindentation tests were further carried out to investigate the nanoscale mechanical heterogeneity after HTC. Fig. 7 (a) is a representative load-displacement ($P$-$h$) curve for the AC sample, and initial yield event (pop-in) is marked by an arrow, which is linked directly to initiation of individual and propagation of SBs and sensitive to soft regions ($H$ and $E_r$ are sensitive to matrix) [37]. Cumulative distributions of $H$ and $E_r$ for the AC, A0.5 and A60 samples are compiled from 49 loading curves, which is shown in Figs. 7(b and c). The AC sample has the lowest average $H$ of 6.6 GPa, followed by 6.8 GPa for A0.5 and 7.2 GPa for A60 sample. The average $E_r$ increases from 111.1 GPa for AC sample to 112.7 GPa for A0.5 and 118.5 GPa for A60 sample. HTC induces local evolution to densely packed atomic structure, resulting in shorter interatomic distances and short-range atomic rearrangement due to structural relaxation and increased $H$ and $E_r$ [38]. This is different from the rejuvenation induced by CTC [17].

Fluctuations of mechanical heterogeneity was further investigated by nanoindentation mapping method. Fig. 8 (a) shows the method for hardness mapping measurements, in which 22 indentation arrays (17 × 17) were performed (together with 6358 indentations from the center to the edge) to acquire hardness distributions at each position. The distance of 150 μm between two neighboring indentation arrays was chosen to avoid the interaction of nearby strained zones. The contour-line maps of nanoindentation hardness are shown in Fig. 8(b–d). Clearly, high hardness areas are surrounded by continuous soft hardness regions and form a relatively continuous grid structure in the A0.5 sample as shown in Fig. 8 (c). Usually a loss in free volume due to structural relaxation tends to cause embrittlement [39,40]. In addition, variation of average hardness values with error bars along the distance from the center was measured and shown in Fig. 8 (e). From the figure, it can be seen the average hardness increases gradually with increasing HTC temperature, consisting with the results of relaxation enthalpy and cumulative distributions of hardness/reduced modulus. However, there exists an abnormally enhanced compressive plasticity after short-term HTC in present study. Herein, we focus on spatially fluctuations of

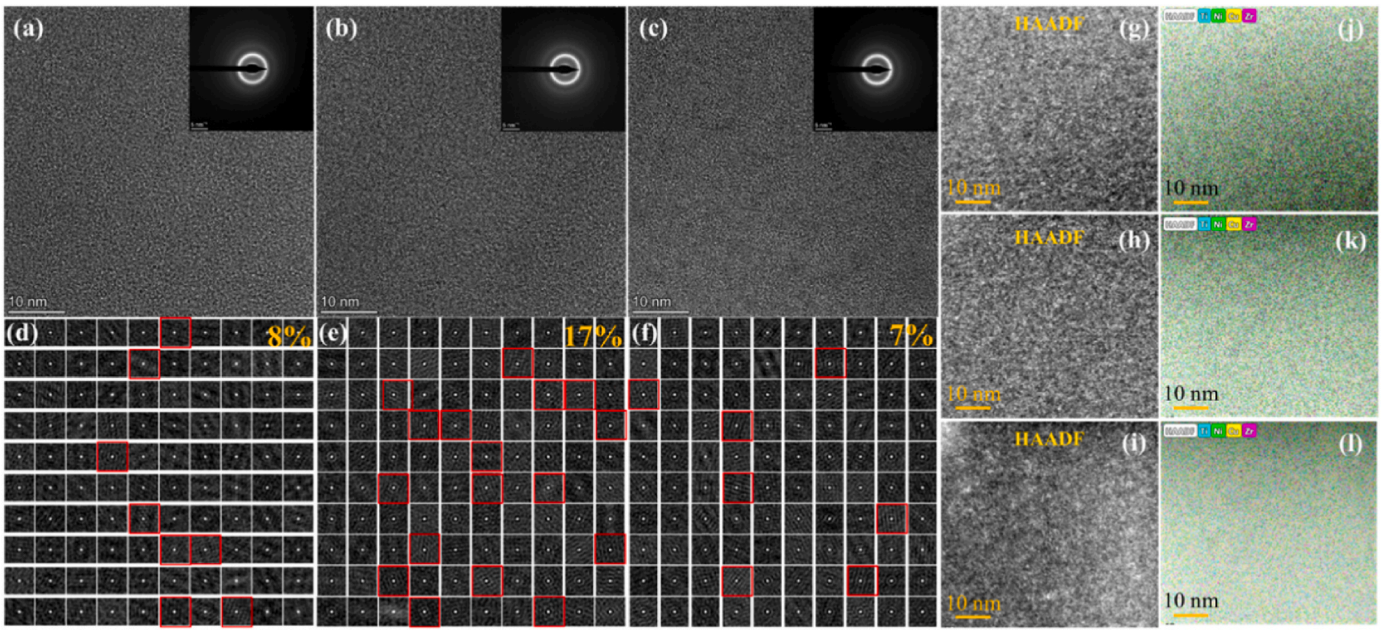


**Fig. 6.** HRTEM images of (a) AC, (b) A0.5 and (c) A60 samples with HTC treatment at 0.98 $T_g$; 2D autocorrelation function of (d) AC, (e) A0.5 and (f) A60 samples with HTC treatment at 0.98 $T_g$; HAADF-TEM images of (g) AC, (h) A0.5 and (i) A60 samples with HTC treatment at 0.98 $T_g$; element mappings of (j) AC, (k) A0.5 and (l) A60 samples with HTC treatment at 0.98 $T_g$.

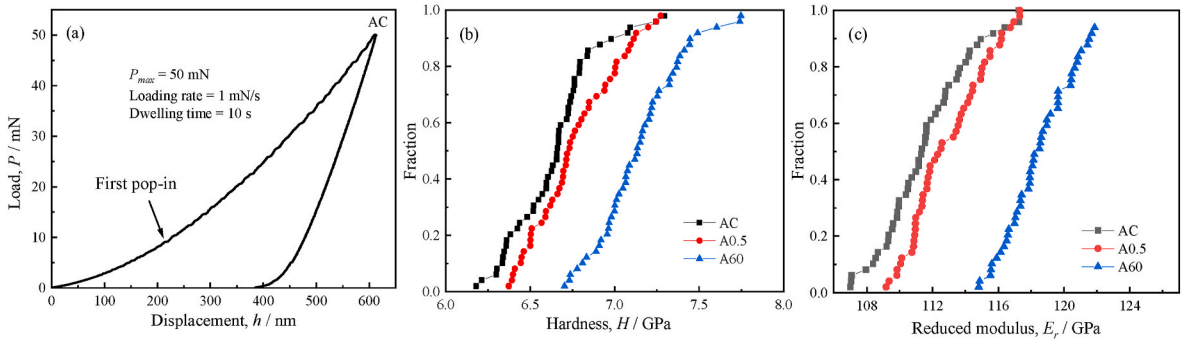


**Fig. 7.** (a) A representative load-displacement curve of AC sample. Cumulative distributions of (b) hardness and (c) reduced modulus for the AC, A0.5 and A60 samples with HTC treatment at 0.98 $T_g$.

hardness (which can be fitted well by Gauss function) and their variation along the direction of radius. As shown in Fig. 8 (f), the full width at half maximum (FWHM) of the first indentation array (the array locates at the center of the sample) of the AC sample can be determined to be 0.27245. The FWHM of hardness of other corresponding indentation arrays with error bars are presented in Fig. 8 (g). It is reported that the hardness fluctuations are accompanied by variations of elastic properties and local compression or stretching of atomic bonds during loading, which facilitates the formation and proliferation of shear bands and also regards as a reflection of structural fluctuations of the materials [41]. For the A0.5 sample, with increasing distance from the center, the FWHM first increases and then shows a serration pattern. The FWHM values of the A0.5 sample are 0.135 and 0.115 for the edge and center position, respectively. Obviously, the FWHM fluctuation of the A0.5 BMG is substantially larger and more obvious compared to AC and A60 samples, manifesting enhanced structural/mechanical fluctuations. The change of FWHM values of hardness (from the center to the edges) is clearly due to different degrees of structural fluctuations during HTC. For A 0.5 sample, the temperature reached during HTC is likely to be different in the center than in the edges as there is no time for thermal equilibration inside the sample. It is worth noting that the FWHM values of A60 are relatively lower than the other two samples for all the investigated positions, indicating the most homogenous structure after long isothermal annealing. These hardness fluctuations suggest that by adjusting the holding time of isothermal annealing, a potentially low-cost manufacturing process for the scalable production of tunable plasticity of BMGs can be proposed.

### 3.3. Nanoscale creep deformation behavior

To further understand the largest FWHM at the edge regions of the A0.5 sample, creep tests are conducted at these regions. Creep can connect internal flow units with external mechanical properties of BMGs in plastically shearing events [35]. Fig. 9 (a) shows typical creep displacement-time curves of the AC sample at different loading rates. With loading rates increasing, the creep depth increases, which is similar to the results observed in other BMGs [42]. Maximum creep displacement of AC, A0.5, and A60 is 7.4, 5.4 and 4.5 nm at a loading rate of 0.5 mN/s, respectively. Decreased creep displacement demonstrates a less pronounced creep deformation after annealing treatment, consisting with previous findings that annealed BMGs with less free volume or higher hardness exhibit better creep resistance [43].

Based on core-shell model, nanoscale heterogeneity can be characterized by two relaxation processes with different relaxation time during

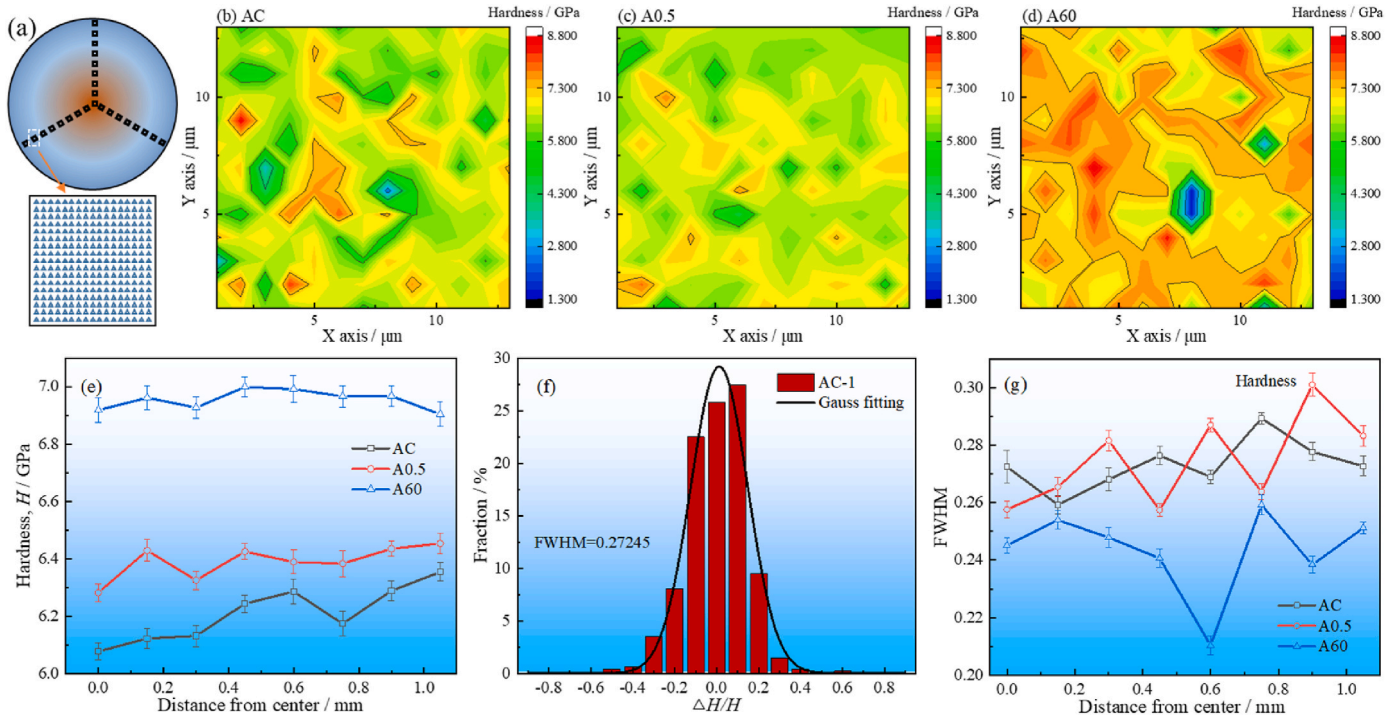


**Fig. 8.** (a) The method for hardness measurements along various circles; contour-line maps of nanoindentation hardness of (b) AC, (c) A0.5 and (d) A60 samples with HTC treatment at 0.98 $T_g$; (e) variation of average hardness value with error bars along the distance from the center of AC, A0.5 and A60 samples; (f) statistical $\Delta H/H$ data of AC sample; (g) the mean FWHM of hardness with error bars of AC, A0.5 and A60 samples with HTC treatment at 0.98 $T_g$.

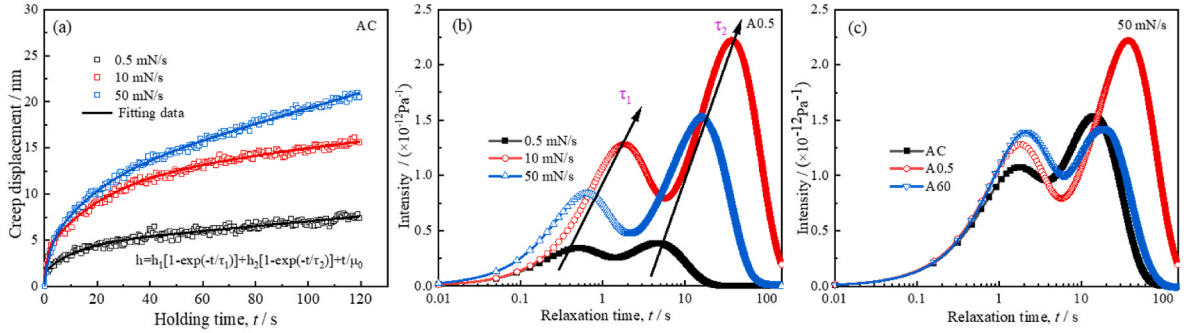


**Fig. 9.** (a) Experimental and fitting creep curves of AC sample; (b) relaxation spectra of (b) A0.5 sample and (c) AC, A0.5 and A60 samples with HTC treatment at 0.98 $T_g$ under the loading rate of 50 mN/s.

creep deformation [44]. Creep curves are analyzed using Maxwell-Voigt model containing Maxwell units and Kelvin units in series. BMGs are structurally heterogeneous at nano to micro-scale [45]. Therefore, a Maxwell unit with 2 K units, i.e., $i = 2$, are utilized, which can well describe creep deformation of viscoelastic materials during an indentation process. Accordingly, creep displacement can be expressed below [42]:

$$h(t) = \sum_{i=1}^{n} h_i\left(1-e^{-t/\tau_i}\right) + t \Big/ \mu_0 \tag{6}$$

where $h_i$ is the indentation depth, $t$ the experimental time during holding segment, $\tau_i$ the characteristic relaxation time of the *i-th* anelastic Kelvin unit, and $\mu_0$ a constant of Maxwell unit. As shown in Fig. 9 (a), creep curves of the AC sample with different loading rates can be fitted well with Eq. (6). The $\mu_0$ as an indicator of visco-plastic deformation of the sample, seems independent of loading rates.

Furthermore, relaxation time spectrum $L(\tau)$, obtained from creep curve can accurately described the two anelastic creep processes of MGs as following expression [46]:

$$L(\tau) = \left(\sum_{i=1}^{n}\left(1+\frac{t}{\tau_i}\right)\frac{h_i}{\tau_i}e^{-t/\tau_i}\right)\frac{A_0}{P_0 h_{in}}t \tag{7}$$

where $A_0/P_0$ is an inverse of hardness, and $h_{in}$ the maximum indentation depth. Fig. 9 (b) presents the relaxation time spectra of A0.5, all of which exhibit two separate relaxation peaks. The first peak with short relaxation time ($\tau_1$) represents smaller defects, while the second peak with long relaxation time ($\tau_2$) represents larger defects [46]. It can be found that when loading rates increases from 0.5 to 10 mN/s, the intensity of both first and secondary peaks increases simultaneously. This phenomenon was also observed in other Fe-based [42] and Zr-based BMGs [46], revealing that more free volume or defects are activated at room temperature in a low-velocity impact mode [46]. The intensity of relaxation spectrum is reduced at the loading rate of 50 mN/s. From equation (7), $L(\tau)$ is not only related to loading rates, but also relates to hardness and characteristic relaxation time. In fact, these mismatch between creep displacement and intensities of $L(\tau)$ were observed in CoFe-based [47],

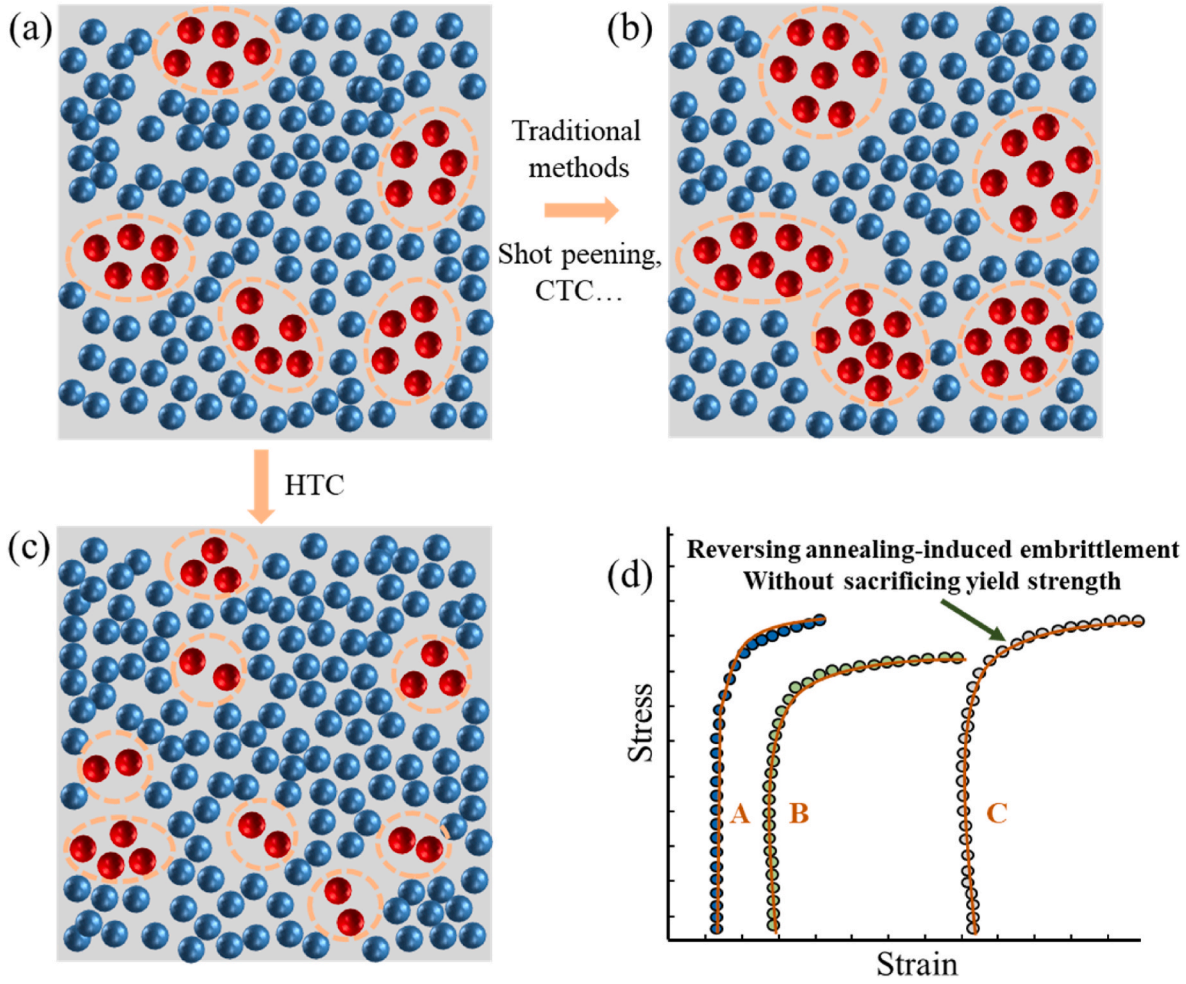


**Fig. 10.** Schematic illustration of two ways to enhance structural heterogeneity of BMGs. Atomic structures for (a) AC, (b) CTC or shot peening and (c) HTC samples; (d) Stress-strain curves of AC, CTC or shot peening and HTC samples. The blue spheres represent atoms in solid-like regions and the red spheres represent atoms in STZs, which are circled in orange dashed ovals.

FeTb-based [48] and Zr-based [32,46] BMGs. Fig. 9 (c) compares relaxation spectra of three samples at a loading rate of 50 mN/s. For A0.5, intensities of both peaks are correspondingly higher than those of the AC sample, and the peak of the secondary relaxation is more intense than the primary relaxation. It is noticed that the higher the peak intensity, the more relaxation processes involved, i.e., more defects of larger size are activated, which may be related with the more obvious structural fluctuations in Fig. 8 (g). For the A60 sample showing a similar plastic strain with the as-cast alloy, the intensity of the first peak shows an obvious increase while the intensity of the second peak (arising from the activation of larger defects) closes to that of the AC sample. This may imply that larger defects with longer relaxation time play a more important role on the plastic deformation.

## 4. Discussion

As shown in Fig. 10 (a), BMGs are composed of liquid-like atoms (red spheres) with lower density and solid-like atoms (blue spheres) with higher density, with different atomic arrangements to external agitations [39]. The low-density regions can be more easily activated under external stress. That is, shear transformation occurs there and STZs form in these regions, which are circled in orange dashed ellipses in Fig. 10 (a). Traditional property manipulation routes, such as CTC or short peening, are widely adopted to improve the plasticity of BMGs via increasing the structural heterogeneity (shown in Fig. 10 (b)) [17,49]. However, the thermal stability and yield strength/hardness are usually reduced due to the introduction of more loosely packed regions, whose stress-strain curve are shown as curves A and B in Fig. 10 (d) [50].

In contrast, conventional annealing usually induces annihilation of free volumes and a more homogeneous structure, leading to degrading of plasticity [10]. Surprisingly enhanced plasticity is observed by short-term isothermal annealing in present work, reversing the relaxation-induced embrittlement in BMGs. Inspired by gradient metallic glasses (GMGs) with spatially gradient distributed free volume/shear bands, nanoindentation arrays from the center to the edges were conduct to investigate structural gradient [51,52] and average hardness along the specific radius direction were measured, shown in Fig. 8 (e). It is noted that the hardness does exhibit gradient increase, consisting with obvious hardness-value gradient in $Zr_{58}Cu_{22}Fe_8Al_{12}$ BMG in a specific direction [52]. As shown in Fig. 8 (e), a more obvious hardness-value gradient can be seen for the AC sample, followed by A0.5 and A60 samples. However, an increase in plastic strain of A0.5 sample were observed without the increase of the structural gradient, showing that structural gradient is not responsible for the increase in plasticity. Herein, we focus on spatially hardness fluctuations via full width at half maximum (FWHM) of nanoindentation arrays along the direction of radius. Hence, this reversal enhanced $\varepsilon_p$ of A0.5 sample is closely associated with the enhanced fluctuation of the FWHM of the hardness' distribution (Fig. 8 (g)) [53], which is different from the usually observed annealing-induced homogeneity. To understand this enhanced degree of mechanical heterogeneity (increased FWHM of the hardness distribution), the effect of heating and cooling processes should be

illustrated (which is usually ignored in conventional annealing for decades of minutes). Similar to the CTC treatment, the fast heating and cooling processes in the HTC can induce local atomic fluctuations and enhance structural fluctuations due to intrinsic non-uniformity of the structure and a non-uniform local coefficient of thermal expansion (CTE) [17,50]. And the holding stage brings about structural relaxation and structural homogeneity, accompanied with annihilation of free volume [54]. Therefore, the plastic strain ($\varepsilon_p$) is the competition between the enhanced heterogeneity caused by cooling/heating and the structural homogeneities arising from relaxation in holding stage. After short-term isothermal annealing, the influence of the structural homogeneity effect cannot eliminate the enhanced heterogeneity caused by cooling/heating, resulting in the enhanced FWHM of the hardness' distribution. With increasing annealing time, the effect of structural homogeneities arising from relaxation in holding stage will dominate over the inhomogeneity effect induced by heating/cooling, leading to the overall homogenization after HTC.

Now, we discuss how the structural variation caused by short-term HTC affects the deformation behavior. First, the enhanced fluctuation of mechanical/structural heterogeneity at different length scales with densification effect leads to the formation of smaller and denser STZs (shown in Fig. 10 (c)) in the A0.5 sample, which is different from CTC treatment (leading to increased heterogeneity with a looser atomic packing in Fig. 10 (b)). These STZs, acting as nucleation site, are prone to form SBs to accommodate more strain. Secondly, the pronounced fluctuations of mechanical/structural heterogeneity at different length scales promote SBs' deflection that fundamentally suppresses the unlimited shear localization, forming multiple shear bands, and endows A0.5 sample with increased plasticity as illustrated in curve C of Fig. 10 (d) [52]. However, when structural relaxation induced by isothermal annealing becomes more dominant with increasing annealing time, the sample becomes mechanically more homogeneous, leading to deteriorated plasticity. Note that a recent work reported a brittle-to-ductile transition induced by a two-step annealing strategy [55]. It was found that thermal treatment of annealing-relaxed BMGs can rejuvenate the BMGs and increase the average volume. Here, we present a novel simpler strategy to enhance the plasticity without rejuvenating the BMGs by single HTC.

## 5. Conclusions

In summary, we show that short-term HTC can enhance structural fluctuations and reverse the annealing induced embrittlement in Zr-based BMGs. Plausible mechanism for such annealing time-regulated plasticity is related to the variation of the structural/mechanical heterogeneity at different length scales. It is revealed that short-term HTC treated sample shows the enhanced fluctuations of the degree of mechanical heterogeneity, i.e., increased degree of mechanical heterogeneity in some positions and decreased degree of mechanical heterogeneity in other positions depending on the distance from the center. This could effectively create more possible STZs activated at high stress, promote the deflection of SBs and form multiple SBs to accommodate the applied stress. HTC with long-term isothermal annealing reduces the degree of mechanical heterogeneity (in terms of FWHM of the hardness' distribution curve) in the whole sample, resulting in embrittlement. These results not only provide a deep understanding of the interplay between structural/mechanical heterogeneity and plasticity, but also offer new strategies for design and optimization of BMGs with desired mechanical performance.

## Author contributions

Q. Luo and B.L. Shen offered Funding acquisition and supervised the project. J.X. Cui. and J.C. He prepared the Zr-based BMGs and performed the annealing treatment. J.X. Cui. and Q. Luo. Formal analysis. Q.Z. Yang assisted in nanoindentation tests. J.X. Cui and Z.G. Zhang. contributed to the discussion and manuscript preparation.

## Data availability

The data that support the findings of this study are available from the corresponding author upon reasonable request.

## Declaration of competing interest

The authors declare that they have no known competing financial interests or personal relationships that could have appeared to influence the work reported in this paper.

## Acknowledgments

This work was supported by the National Natural Science Foundation of China (Grant Nos. 51971061 and 52231005) and Natural Science Foundation of Jiangsu Province (Grant No. BK20221474).

## References

[1] Zhang ZF, Wang CY, Liu P, Reddy KM, Wang XD, Chen MW, et al. Deformation behavior of a nanoporous metallic glass at room temperature. Int J Plast 2022;152:103232. https://doi.org/10.1016/j.ijplas.2022.103232.
[2] Bai FX, Yao JH, Wang YX, Pan J, Li Y. Crystallization kinetics of an Au-based metallic glass upon ultrafast heating and cooling. Scripta Mater 2017;132:58–62. https://doi.org/10.1016/j.scriptamat.2017.02.001.
[3] Li BS, Xie S, Kruzic JJ. Toughness enhancement and heterogeneous softening of a cryogenically cycled Zr-Cu-Ni-Al-Nb bulk metallic glass. Acta Mater 2019;176:278–88. https://doi.org/10.1016/j.actamat.2019.07.012.
[4] Liontas R, Zadeh MJ, Zeng QS, Zhang YW, Mao WL, Greer JR. Substantial tensile ductility in sputtered Zr-Ni-Al nano-sized metallic glass. Acta Mater 2016;118:270–85. https://doi.org/10.1016/j.actamat.2016.07.050.
[5] Ghidelli M, Orekhov A, Bassi AL, Terraneo G, Djemia P, Abadias G, et al. Novel class of nanostructured metallic glass films with superior and tunable mechanical properties. Acta Mater 2021;213:116955. https://doi.org/10.1016/j.actamat.2021.116955.
[6] Yang JM, Zhao ZY, Mu J, Wang YD. Effect of pre-plastic-deformation on mechanical properties of TiZr-based amorphous alloy composites. Mater. Sci. Eng. A 2018;716:23–7. https://doi.org/10.16339/j.cnki.hdxbzkb.2017.06.003.
[7] Luo P, Zhu F, Lv YM, Lu Z, Shen LQ, Zhao R, et al. Microscopic structural evolution during ultrastable metallic glass formation. ACS Appl Mater Interfaces 2021;13:40098–105. https://doi.org/10.1021/acsami.1c10716.
[8] Garrett GR, Demetriou MD, Launey ME, Johnson WL. Origin of embrittlement in metallic glasses. P. Natl. Acad. Sci. USA. 2016;113:10257–62. https://doi.org/10.1073/pnas.1610920113.
[9] Murial P, Ramamurty U. Embrittlement of a bulk metallic glass due to sub-$T_g$ annealing. Acta Mater 2005;53:1467–78. https://doi.org/10.1016/j.actamat.2004.11.040.
[10] Minner C, Kuhnt M, Bruns S, Marshal A, Pradeep KG, Marsilius M, et al. Study on the embrittlement of flash annealed $Fe_{85.2}B_{9.5}P_4Cu_{0.8}Si_{0.5}$ metallic glass ribbons. Mater Des 2018;156:252–61. https://doi.org/10.1016/j.matdes.2018.06.055.
[11] Gao M, Kursun C, Perepezko JH. Unrevealing structural relaxation induced ductile-to brittle transition from perspective of shear band nucleation kinetics in metallic glass. J Alloys Compd 2023;952:170022. https://doi.org/10.1016/j.jallcom.2023.170022.
[12] Malekan M, Rashidi R, Shabestari SG. Mechanical properties and crystallization kinetics of Er-containing Cu-Zr-Al bulk metallic glasses with excellent glass forming ability. Vacuum 2020;174:109223. https://doi.org/10.1016/j.vacuum.2020.109223.
[13] Wang T, Zhou YL, Zhang LS. Chemical and structural heterogeneity improve the plasticity of a Zr-based bulk metallic glass at low-temperature annealing. J Non-Cryst Solids 2023;603:122115. https://doi.org/10.1016/j.jnoncrysol.2022.122115.
[14] Saini P, Narayan RL. On simultaneous enhancement in local yield strength and plasticity of short-term annealed bulk metallic glasses. J Alloys Compd 2022;898:162960. https://doi.org/10.1016/j.jallcom.2021.162960.
[15] Di SY, Wang QQ, Yang YY, Liang T, Zhou J, Su L, et al. Efficient rejuvenation of heterogeneous $\{[(Fe_{0.5}Co_{0.5})_{0.75}B_{0.2}Si_{0.05}]_{96}Nb_4\}_{99.9}Cu_{0.1}$ bulk metallic glass upon cryogenic cycling treatment. J Mater Sci Technol 2022;97:20–8. https://doi.org/10.1016/j.jmst.2021.04.034.
[16] Huang B, Tang XC, Geng C, He QF, Yi J, Wang Q, et al. Hidden shear bands of diversified structures in a bent heterogeneous metallic glass. Mater. Sci. Eng. A 2023;869:144726. https://doi.org/10.1016/j.msea.2023.144726.
[17] Ketov SV, Sun YH, Nachum S, Lu Z, Checchi A, Beraldin AR, et al. Rejuvenation of metallic glasses by non-affine thermal strain. Nature 2015;524:200–3. https://doi.org/10.1038/nature14674.
[18] Cui JX, Luo Q, Zhang ZG, Zhu JT, Shen BL. Tailoring mechanical heterogeneity, nanoscale creep deformation and optical properties of nanostructured Zr-based

metallic glass. Rare Met 2023;42:3430–42. https://doi.org/10.1007/s12598-023-02440-8.
[19] Wang LL, Wang Z, Chu W, Zhao X, Hu LN. Evolution path of metallic glasses under extensive cryogenic thermal cycling: rejuvenation or relaxation? Mater. Sci. Eng. A 2022;850:143551. https://doi.org/10.1016/j.msea.2022.143551.
[20] Li MC, Guan HM. Unified upper temperature for cryogenic thermal cycling treatment in Fe-based metallic glasses. J Alloys Compd 2023;931:167263. https://doi.org/10.1016/j.jallcom.2022.167263.
[21] Costa MB, Londono JJ, Blatter A, Hariharan A, Gerert A, Carpenter MA, et al. Anelastic-like nature of the rejuvenation of metallic glasses by cryogenic thermal cycling. Acta Mater 2023;244:118551. https://doi.org/10.1016/j.actamat.2022.118551.
[22] Feng SD, Chan KC, Zhao L, Pan SP, Qi L, Wang LM, et al. Rejuvenation by weakening the medium range order in $Zr_{46}Cu_{46}Al_8$ metallic glass with pressure preloading: a molecular dynamics simulation study. Mater Des 2018;158:248–55. https://doi.org/10.1016/j.matdes.2018.08.040.
[23] Lv ZW, Wei C, Zhang S, Shi ZL, Zhang HR, Zhang XY, et al. Microstructure and mechanical behavior evolution of Ti-based bulk metallic glass induced by sub-$T_g$ isothermal annealing. J Alloys Compd 2022;900:163300. https://doi.org/10.1016/j.jallcom.2021.163300.
[24] Di SY, Wang QQ, Zhou J, Shen YY, Li JQ, et al. Enhancement of plasticity for FeCoBSiNb bulk metallic glass with superhigh strength through cryogenic thermal cycling. Scripta Mater 2020;187:13–8. https://doi.org/10.1016/j.scriptamat.2020.05.059.
[25] Song M, Liao X, He Y. Effect of sub-$T_g$ annealing on the mechanical properties of a ZrAlNiCuNb bulk metallic glass. Phil Mag Lett 2011;91:713–23. https://doi.org/10.1080/09500839.2011.609842.
[26] Spaepen F. Structural model for solid-liquid interface in monatomic systems. Acta Mater 1975;23:729–43. https://doi.org/10.1016/0001-6160(75)90056-5.
[27] Argon AS, Salama M. The Mechanism of fracture in glassy materials capable of some inelastic deformation. Mater. Sci. Eng. 1976;23:219–30. https://doi.org/10.1016/0025-5416(76)90198-1.
[28] Wu FF, Zheng W, Wu SD, Zhang ZF, Shen J. Shear stability of metallic glasses. Int J Plast 2011;27:560–75. https://doi.org/10.1016/j.ijplas.2010.08.004.
[29] Shi HQ, Tang CC, Zhao XY, Ding Y, Ma LQ, Shen XD. Effect of isothermal annealing on mechanical performance and corrosion resistance of Ni-free $Zr_{59}Ti_6Cu_{17.5}Fe_{10}Al_{7.5}$ bulk metallic glass. J Non-Cryst Solids 2020;537:120013. https://doi.org/10.1016/j.jnoncrysol.2020.120013.
[30] Zhou M, Hagos K, Huang HZ, Yang M, Ma LQ. Improved mechanical properties and pitting corrosion resistance of $Zr_{65}Cu_{17.5}Fe_{10}Al_{7.5}$ bulk metallic glass by isothermal annealing. J Non-Cryst Solids 2016;452:50–6. https://doi.org/10.1016/j.jnoncrysol.2016.08.014.
[31] Song SX, Zhu F, Chen MW. Universal scaling law of glass rheology. Nat Mater 2022;21:404–9. https://doi.org/10.1038/s41563-021-01185-y.
[32] Liu SQ, Chang ZX, Fu YQ, Liu YY, Lin MC, Ren XB, et al. Nanoscale creep behavior and its size dependency of a Zr-based bulk metallic glass manufactured by selective laser melting. Mater Des 2011;218:110723. https://doi.org/10.1016/j.matdes.2022.110723.
[33] Tao K, Li FC, Liu YH, Pineda E, Song KK, Qiao JC. Unraveling the microstructural heterogeneity and plasticity of $Zr_{50}Cu_{40}Al_{10}$ bulk metallic glass by nanoindentation. Int J Plast 2022;154:103305. https://doi.org/10.1016/j.ijplas.2022.103305.
[34] Guo H, Jiang CB, Yang BJ, Wang JQ. Deformation behavior of Al-rich metallic glasses under nanoindentation. J Mater Sci Technol 2017;33:1272–7. https://doi.org/10.1016/j.jmst.2016.10.014.
[35] Sahu BP, Dutta A, Mitra R. Mechanism of negative strain rate sensitivity in metallic glass film. J Alloys Compd 2019;784:488–99. https://doi.org/10.1016/j.jmst.2016.10.014.
[36] Luo P, Cao CR, Zhu F, Lv YM, Liu YH, Wen P, et al. Ultrastable metallic glasses formed on cold substrates. Nat Commun 2018;9:1389. https://doi.org/10.1038/s41467-018-03656-4.
[37] Meylan CM, Greer AL. The effects of elastic cycling in nanoindentation of a metallic glass. Phil Mag 2020;100:3141–54. https://doi.org/10.1080/14786435.2020.1814494.
[38] Brechtl J, Wang H, Kumar NA, Lin T, Rbei Y, Neuefeind H, et al. Investigation of the thermal and neutron irradiation response of BAM-11 bulk metallic glass. J Nucl Mater 2019;526:151771. https://doi.org/10.1016/j.jnucmat.2019.151771.
[39] Cui JX, Luo Q, Di SY, Zhang ZG, Shen BL. Rejuvenation-to-relaxation transition induced by elastostatic compression and its effect on deformation behavior in a Zr-based bulk metallic glass. Metals 2022;12:282. https://doi.org/10.3390/met12020282.
[40] Ramamurty U, Lee ML, Basu J, Li Y. Embrittlement of a bulk metallic glass due to low temperature annealing. Scripta Mater 2002;47:107–11. https://doi.org/10.1016/S1359-6462(02)00102-1.
[41] Riechers B, Ott C, Das SM, Liebsher CH, Samwer K, Derlet PM, et al. On the elastic microstructure of bulk metallic glasses. Mater Des 2023;229:111929. https://doi.org/10.1016/j.matdes.2023.111929.
[42] Yoo BG, Kim JY, Kim YJ, Choi IC, Shim S, Ting Y, et al. Increased time-dependent room temperature plasticity in metallic glass nanopillars and its size-dependency. Int J Plast 2012;37:108–18. https://doi.org/10.1016/j.ijplas.2012.04.005.
[43] Wang WH, Wang RJ, Yang WT, Wei BC, Wen P, Zhao DQ, et al. Stability of ZrTiCuNiBe bulk metallic glass upon isothermal annealing near the glass transition temperature. J Mater Res 2011;17:1385–9. https://doi.org/10.1557/JMR.2002.0206.
[44] Ke HB, Zeng JF, Liu CT, Yang Y. Structure heterogeneity in metallic glass: modeling and Experiment. J Mater Sci Technol 2014;30:560–5. https://doi.org/10.1016/j.jmst.2013.11.014.
[45] Zhu F, Song SX, Reddy KM, Hirata A, Chen MW. Spatial heterogeneity as the structure feature for structure-property relationship of metallic glasses. Nat Commun 2018;9:3965. https://doi.org/10.1016/j.jmst.2013.11.014.
[46] Yuan CC, Lv ZW, Pang CM, Li Xin, Liu R, Yang C, et al. Ultrasonic-assisted plastic flow in a Zr-based metallic glass. Sci China Mater 2020;64:448–59. https://doi.org/10.1007/s40843-020-1411-2.
[47] Lv ZW, Yuan CC, Ke HB, Shen BL. Defects activation in CoFe-based metallic glasses during creep deformation. J Mater Sci Technol 2021;69:42–7. https://doi.org/10.1016/j.jmst.2020.08.012.
[48] Yuan CC, Liu R, Pang CM, Zuo XF, Li BF, Song SC, et al. Anelastic and viscoplastic deformation in a Fe-based metallic glass. J Alloys Compd 2021;853:157233. https://doi.org/10.1016/j.jallcom.2020.157233.
[49] Zhang Y, Wang WH, Greer AL. Making metallic glasses plastic by control of residual stress. Nat Mater 2006;5:857–60. https://doi.org/10.1038/nmat1758.
[50] Wu Y, Cao D, Yao YL, Zhang GS, Wang JY, Liu LQ, et al. Substantially enhanced plasticity of bulk metallic glasses by densifying local atomic packing. Nat Commun 2021;12. https://doi.org/10.1038/s41467-021-26858-9.
[51] Ryu W, Yamada R, Saida J. Tailored hardening of ZrCuAl bulk metallic glass induced by 2D gradient rejuvenation. NPG Asia Mater 2020;12:52. https://doi.org/10.1038/s41427-020-0233-8.
[52] Tang Y, Zhou HF, Lu HM, Wang XD, Cao QP, Zhang DX, et al. Extra plasticity governed by shear band deflection in gradient metallic glasses. Nat Commun 2022;13:2120. https://doi.org/10.1038/s41467-022-29821-4.
[53] Şopu D, Scudino S, Bian XL, Gammer C, Eckert J. Atomic-scale origin of shear band multiplication in heterogeneous metallic glasses. Scripta Mater 2020;178:57–61. https://doi.org/10.1016/j.scriptamat.2019.11.006.
[54] Yang M, Liu XJ, Wu Y, Wang H, Wang JB, Ruan HH, et al. Elastic modulus change and its relation with glass-forming ability and plasticity in bulk metallic glasses. Scripta Mater 2019;161:62–5. https://doi.org/10.1016/j.scriptamat.2018.10.006.
[55] Meng YH, Zhang SY, Zhou WH, Hao JH, Liu SN, Lan S, et al. Rejuvanation by enthalpy relaxation in metallic glasses. Acta Mater 2022;241:118376. https://doi.org/10.1016/j.actamat.2022.118376.